



Regulating Pt electronic properties on NiFe layered double hydroxide interface for highly efficient alkaline water splitting

Lei Tan^{a,b,1}, Haifeng Wang^{b,1}, Chunhong Qi^{b,1}, Xuan Peng^b, Xiangxiang Pan^b, Xiaotong Wu^b, Zekun Wang^a, Lin Ye^a, Qi Xiao^b, Wei Luo^b, Hongtao Gao^a, Wanguo Hou^c, Xiaopeng Li^{b,*}, Tianrong Zhan^{a,*}

^a Key Laboratory of Optic-electric Sensing and Analytical Chemistry for Life Science (Ministry of Education), College of Chemistry and Molecular Engineering, Qingdao University of Science and Technology, Qingdao 266042, China

^b State Key Laboratory for Modification of Chemical Fibers and Polymer Materials & College of Materials Science and Engineering, Donghua University, Shanghai 201620, China

^c Key Laboratory of Colloid & Interface Chemistry (Ministry of Education), Shandong University, Jinan 250100, China

ARTICLE INFO

Keywords:

Electrocatalysis
Oxygen evolution reaction
Hydrogen evolution reaction
Water splitting
Layered double hydroxide
Pt electronic regulation

ABSTRACT

Developing cost-effective and highly efficient oxygen evolution reaction (OER) and hydrogen evolution reaction (HER) electrocatalysts is imperative for catalyzing water electrolysis. In this study, significant change in Pt electronic properties was conducted on NiFe layered double hydroxide (NiFe-LDH) by simply regulating the order of boron-modification and Pt-deposition, thereby achieving two electrocatalysts of B-Pt-NiFe-LDH with major Pt⁰ species and Pt-B-NiFe-LDH with Pt²⁺ species as the main component, respectively. Interestingly, the B-Pt-NiFe-LDH electrocatalyst displays better alkaline OER performance with a smaller overpotential (208 mV) at 100 mA cm⁻² than Pt-B-NiFe-LDH (229 mV), while the Pt-B-NiFe-LDH electrocatalyst shows superior alkaline HER performance with only 19 mV overpotential at 10 mA cm⁻² compared with that of B-Pt-NiFe-LDH (65 mV) and Pt-NiFe-LDH (28 mV). The corresponding electrolyzer of B-Pt-NiFe-LDH//Pt-B-NiFe-LDH in 1 M KOH requires only a very low voltage of 1.475 V to deliver 10 mA cm⁻² with good durability (110 h), which exceeds the performance of the widely studied RuO₂//Pt/C cell (1.516 V). Density functional theory (DFT) calculations suggest that the Pt⁰ species on NiFe-LDH can lower the energy barrier for OER, while the Pt^{2+/4+} components are beneficial for HER. This work demonstrates the rational strategy to regulate electronic properties on electrocatalysts for highly efficient water-splitting.

1. Introduction

Water electrolysis has gained much attention because it not only can yield high-caloric hydrogen without carbon emission, but also can synchronously store unstable renewable wind, solar, and tidal power, etc [1]. Precious metal-based compounds are accepted as advanced electrocatalysts for water electrolysis (e.g. Ir-/Ru-based and Pt-based catalysts), while their scarcity, instability, and high cost become a stumbling block for their commercialization [2–4]. Consequently, many strategies, such as interface engineering [5,6], strain engineering [7,8], spin-state modulation [9,10], and hybridization engineering [11,12], have been employed to develop low-loading and even zero-loading noble metal electrocatalysts that can enhance oxygen evolution

reaction (OER) at the anode or/and hydrogen evolution reaction (HER) at the cathode [13–15].

Heterostructures based on two-dimensional (2D) materials have been extensively and intensively studied for their multifarious applications in the electrocatalytic field owing to their abundant active sites, large specific surface area, and diverse physicochemical properties [16–21]. Among them, metal/metal (hydro)oxide type heterostructures, existing strong interactions between metal species and substrate due to electronic and lamellar effects, demonstrate better electrocatalytic activity and durability than their parts [22–24]. 2D nanosheets can limit their loadings and increase the dispersion of noble metal active sites in this type of heterostructure.

Platinum (Pt) is a well-recognized catalyst for the cathodic HER due

* Corresponding authors.

E-mail addresses: xiaopeng.li@dhu.edu.cn (X. Li), trzhan@qust.edu.cn (T. Zhan).

¹ These authors contributed equally to this work.

to its optimal hydrogen absorption energy [25–28]. Nevertheless, the Pt catalyst shows poor activity toward the anodic OER since it has an extremely strong affinity with oxygen intermediates [29,30]. Besides, Pt is highly vulnerable in an oxidative environment at comparatively high anodic potentials of 1.4 V vs. reversible hydrogen electrode (RHE) which can lead to the leaching of active Pt species in the electrolyte [31,32]. Although Pt is generally considered to be almost inactive to OER [30], it has been demonstrated to promote the OER activity of transition metal oxides as a co-catalyst by regulating the electronic configuration of active centers [14]. Especially, when Pt occurs in monatomic form, its unique coordination structure combined with strong electronic coupling between separate Pt atoms and neighboring metal and/or nonmetal atoms can greatly advance its OER electrocatalytic performance [13]. Hence, to develop efficient and stable Pt-based OER catalysts, the electronic structure and local coordination environment of Pt should be precisely optimized to accelerate the OER kinetics and prevent active Pt species from being oxidized.

Layered double hydroxides (LDH) are well-known transition metal electrocatalysts for OER because of their ultrathin lamellar structure, the adjustable composition of host layers and interlayer guest species, and intrinsic electrocatalytic activity [33–35]. Particularly, both experimental and theoretical results have demonstrated that NiFe-LDH is the most active for OER and even can act as a benchmark under alkaline conditions [36,37]. Unfortunately, except for inherent low conductivity, pure NiFe-LDH only displays poor HER activity in alkaline electrolytes due to their inferior capability to form hydrogen molecules by recombining hydrogen intermediates (H_{ad}) [38,39]. Furthermore, HER rates of Pt-based catalysts in alkaline environments are significantly lower, often by 2–3 orders of magnitude, compared to their performance in acidic conditions [40,41]. In practical application, however, alkaline HER is an essential component for the application of proton exchange membrane-based water electrolyzers [41–44]. Fortunately, NiFe-LDH is an ideal substrate to anchor sub-nanometer Pt clusters with good dispersion due to its highly ordered hydrotalcite-like layer formed by sharing edges of octahedral MO_6 units [45,46]. The deposition of NiFe-LDH by Pt atoms could improve the OER performance of Pt and the HER performance of NiFe-LDH in alkaline electrolytes [38,45].

On the other hand, the introduction of electron-deficient boron (B) in Ni-based materials can improve the OER performance by promoting the formation and stabilization of the active phase of Ni-oxhydroxides ($NiOOH$) [47–49]. The existence of B species can also upgrade the catalytic performance of surface Pt-group metal sites for many electrocatalytic reactions [50,51]. Given the above-mentioned fundamentals, this work reports a new tactic to prepare OER and HER electrocatalysts that feature the integration of trace Pt and NiFe-LDH with the aid of a boron modification process. Specifically, after the electrodeposition of trace Pt on Ni-foam-supported NiFe-LDH, the subsequent B modification affords the OER catalyst (B-Pt-NiFe-LDH). The electrodeposition of Pt on B-modified NiFe-LDH gives rise to the HER catalyst (Pt-B-NiFe-LDH). For B-Pt-NiFe-LDH, NiFe-LDH is the active center of OER and the heterogeneous interface between the Pt clusters mainly in zero valence and NiFe-LDH further improves the OER performance of the catalyst. For Pt-B-NiFe-LDH, the Pt species mainly in +2 valence are the active center of HER, and B-modified NiFe-LDH acts as a co-catalyst to enhance the electrocatalytic activity and stability towards the HER under alkaline conditions. The electrocatalytic cell with B-Pt-NiFe-LDH//Pt-B-NiFe-LDH displays excellent overall water-splitting performance with an ultralow potential of 1.475 V to achieve 10 mA cm^{-2} current density. The theoretical density functional theory (DFT) calculations proved that the Pt^0 species on NiFe-LDH reduces the energy barrier for OER. The oxidized Pt species on NiFe-LDH contributes to the stabilization of H_2O and OH but leads to easier H-desorption, thus resulting in the best HER performance. This work offers a new strategy to develop low-loading noble metal-based electrocatalysts for water-splitting by interface engineering of 2D materials.

2. Experimental section

2.1. Chemicals and materials.

Nickel foam (NF) was purchased from Shengernuo Technology Co. Ltd (Suzhou, China). $Fe(NO_3)_3 \cdot 9H_2O$ ($\geq 98.5\%$), $Ni(NO_3)_2 \cdot 6H_2O$ ($\geq 98\%$), NH_4F ($\geq 96\%$), Urea ($\geq 99\%$), $NaBH_4$ ($\geq 98\%$), $NaOH$ ($\geq 96\%$), Ethanol (C_2H_6O , $\geq 99.7\%$), KOH ($\geq 85\%$), Hydrochloric acid (HCl, 36.0–38.0%) were purchased from Sinopharm Chemical Reagent Co., Ltd. Chloroplatinic acid hydrate (H_2PtCl_6 , 99.995%) was purchased from Sigma Aldrich. Ultrapure water (resistivity: $18.2\text{ }\Omega\text{m}$) was applied throughout the whole experiment. All the reagents were of analytical grade and used without additional purification.

2.2. Synthesis of NiFe-LDH.

The synthesis procedure followed a method recorded in a previous study [6]. Initially, a piece of commercial nickel foam ($2 \times 3\text{ cm}^2$) underwent sequential ultrasonic treatment with a 1 M HCl aqueous solution, followed by ultra-pure water, and then ethanol, each for durations of 30, 5, and 10 min, respectively, to eliminate impurities. Subsequently, a solution composed of 0.33 mmol $Fe(NO_3)_3 \cdot 9H_2O$, 0.67 mmol $Ni(NO_3)_2 \cdot 6H_2O$, and 5 mmol urea in 30 mL ultrapure water was stirred for 30 min. NH_4F (5 mmol) was introduced to the solution and stirred for an additional 30 min. The resulting mixture was transferred into a Teflon autoclave for 12 h at $120\text{ }^\circ\text{C}$. After the autoclave naturally cooled to room temperature, the NF was rinsed multiple times with distilled water and ethanol to get rid of excessive materials on the surface followed by vacuum drying at $50\text{ }^\circ\text{C}$ for 6 h. Finally, the resulting electrode precursor was identified as NiFe-LDH.

2.3. Synthesis of B-NiFe-LDH.

To synthesize boron-modified NiFe-LDH (B-NiFe-LDH), the as-prepared NiFe-LDH precursor was soaked in 20 mL 0.5 M $NaBH_4$ aqueous solution along with 1 M $NaOH$ to slow down the hydrolysis of $NaBH_4$, at room temperature for 1 h to ensure the complete reaction. After this step, the B-NiFe-LDH catalyst was obtained after washing and then drying in a vacuum. The influence of the B-modification extent was investigated by changing $NaBH_4$ concentrations (0.1, 0.2, 0.5, 1.0, and 2.0 M). $NaBH_4$ serves both as the reducing agent as well as the boron source in this reaction.

2.4. Synthesis of Pt-NiFe-LDH.

The electrodeposition of Pt was implemented in a typical three-electrode cell, in which the NiFe-LDH ($1 \times 2\text{ cm}^2$) serves as the working electrode, and platinum sheet and Hg/HgO electrode are used as the counter and reference electrode, respectively. The electrolyte is a 30 mL aqueous solution of H_2PtCl_6 (12 mg). The electrodeposition is performed by cyclic voltammetry (CV) scanning for 50 cycles under a potential range from -0.5 – 0.4 V (vs. Hg/HgO) at the scan rate of 20 mV s^{-1} . Then the Pt-NiFe-LDH electrode was obtained after being rinsed with water and dried in a vacuum at $60\text{ }^\circ\text{C}$. The different scanning cycles (30, 40, 60, and 100 cycles) for the electrodeposition were also determined to optimize this parameter.

2.5. Synthesis of Pt-B-NiFe-LDH.

The Pt-B-NiFe-LDH catalyst was synthesized in the light of a similar procedure to that of Pt-NiFe-LDH, in which NiFe-LDH was replaced by B-NiFe-LDH.

2.6. Synthesis of B-Pt-NiFe-LDH.

The B-Pt-NiFe-LDH electrode was prepared according to a similar

procedure to that of B-NiFe-LDH, in which NiFe-LDH was replaced by Pt-NiFe-LDH.

2.7. Synthesis of Pt-NF.

The Pt-NF electrode was prepared by directly depositing Pt on NF under the same electrodeposition conditions.

3. Results and discussion

3.1. Structural characterization

The synthetic route of B-Pt-NiFe-LDH and Pt-B-NiFe-LDH electrodes is illustrated in Fig. 1. Firstly, the NiFe-LDH catalyst was synthesized via a conventional hydrothermal coprecipitation on a porous NF substrate that can provide high conductivity and a large surface area [52–55]. The green self-standing NiFe-LDH (Fig. S1) was then treated in a basic NaBH_4 solution at room temperature to obtain B-NiFe-LDH. The B-modification was tuned by varying the concentration of the NaBH_4 solution. As shown in Fig. S2, these B-NiFe-LDH products keep almost equal lamellar morphologies but with a slightly thinner thickness relative to the NiFe-LDH precursor. Among them, the B-NiFe-LDH based on 0.5 M NaBH_4 solution presents the best OER activity (Fig. S3) and this concentration was employed for all B-modification treatments in this study. To prepare B-Pt-NiFe-LDH, Pt-NiFe-LDH was first synthesized by stably depositing Pt on NiFe-LDH using a CV method [56]. To gain the best OER activity of Pt-NiFe-LDH, the Pt loadings were optimized by adjusting the CV cycle number of the electrodeposition (Fig. S4). Under the optimal condition, the appropriate Pt loading can ensure the even distribution of Pt species on the nanosheets and avoid the coverage of NiFe-LDH active sites by excess Pt load (Fig. S5). The Pt-NiFe-LDH by depositing 50 CVs displays the best activity and this cycle number is thus used for the deposition of Pt. Due to the small size and trace load of the Pt component, we did not find a distinct morphology difference between Pt-NiFe-LDH and NiFe-LDH (Fig. S5). B-Pt-NiFe-LDH was obtained by processing Pt-NiFe-LDH in a basic NaBH_4 solution, during which a large number of bubbles was generated from the self-supported electrode (Video S1). Compared with the mild B-modification toward NiFe-LDH (no obvious bubbles, Video S1), this more violent reaction could be ascribed to the reduction of high-valence Pt species to lower-valence forms by NaBH_4 [57]. The Pt-B-NiFe-LDH electrode was prepared by directly depositing Pt on B-NiFe-LDH under the same condition. The SEM images of B-Pt-NiFe-LDH (Fig. 2d and Fig. S6) reveal the visible flocculent layer on the nanosheet surfaces of Pt-NiFe-LDH. However, the post-deposition of Pt results in relatively smooth surfaces with thinner thickness of nanoflakes in Pt-B-NiFe-LDH (Fig. 2e and Fig. S7) than in B-Pt-NiFe-LDH. The fine structures of these two catalysts were characterized by transmission

electron microscopy (TEM) and high-angle annular dark field-scanning transmission electron microscopy (HAADF-STEM). As presented in Figs. 2h and 2n, for both samples, the B-modification and Pt-deposition in a different sequence gave rise to insignificant effects on the morphology of the NiFe-LDH nanosheets. HRTEM images of two catalysts display the (012) plane of NiFe-LDH with lattice distances of about 0.262 ~ 0.265 nm (Figs. 2i, 2j, and 2p). There is a large number of Pt clusters (marked by yellow ellipses) with a diameter of about 2.5 nm on nanosheets (Figs. 2f–2g) for B-Pt-NiFe-LDH, which could be ascribed to the reduction of Pt species by NaBH_4 . However, fewer Pt clusters were found for Pt-B-NiFe-LDH (Figs. 2l–2m) because some Pt species mainly occur in the forms of Pt^{2+} with part of Pt^0 due to the absence of the post-reduction procedure. As shown in Figs. 2i and 2o, the lattice distances of 0.228 and 0.224 nm are assigned to the (111) plane of Pt, which is considered to be the existence of Pt^0 in both catalysts. No distinct lattice fingers for Pt^{2+} and Pt^{4+} were observed in Pt-B-NiFe-LDH probably due to a low percentage (Fig. 2n). The EDS elemental mapping images in Figs. 2k and 2q imply the uniform distribution of Ni, Fe, Pt, B, and O in these two catalysts. The relatively low B contents (0.08 at ~1.57 at%) in two catalysts (Table S1) reveal only the surface B modification rather than a phase transformation by the action of NaBH_4 . The B-modification can result in partial amorphousness of NiFe-LDH, which can enhance the OER catalytic activity and stability of the catalysts [58].

The phase structures of all catalysts were identified by XRD patterns as shown in Fig. 3a. All catalysts exhibit the characteristic (003), (006), (101), (012), (015), (110), and (113) diffraction peaks matched with the NiFe-LDH (JCPDS: 40–0215) along with a $\beta\text{-Ni}(\text{OH})_2$ (JCPDS 14–0117) peak at 19.8° . Besides, the three strong peaks are indexed to the NF substrate (JCPDS 04–0850). However, the B-modified product exhibits a lower intensity and slightly wider peak width than their precursors (B-NiFe-LDH vs. NiFe-LDH, B-Pt-NiFe-LDH vs. Pt-NiFe-LDH, and Pt-B-NiFe-LDH vs. NiFe-LDH), disclosing that the modification by boron resulted in the decreased crystallinity of the LDH phase, which may be due to the formation of amorphous surface structure [59,60]. The absence of a Pt-related diffraction peak signifies the small size of Pt nanoclusters and low Pt loading (ICP-OES: ≤ 1.019 wt%) in the three black Pt-based catalysts (Fig. S2). The Raman spectrum of these catalysts presents the typical $E_{g(R)}$, A_{1g} , and $E_{g(T)}$ modes of the NiFe-LDH phase at around 300, 450, and 535 cm^{-1} , respectively [35,61] (Fig. S11). The B-modification or/and Pt deposition produce a red-shift of the A_{1g} and $E_{g(T)}$ peaks with an increased peak width. This observation means that B modification or Pt deposition can usually result in either the crystallinity change or the lattice strain or stress [62–64]. These surface modifications are conducive to better electrocatalytic performance.

X-ray photoelectron spectroscopy (XPS) measurements were carried out to further analyze the elemental surface states and electronic characteristics of all catalysts. The XPS survey spectra (Fig. S12a) showed the

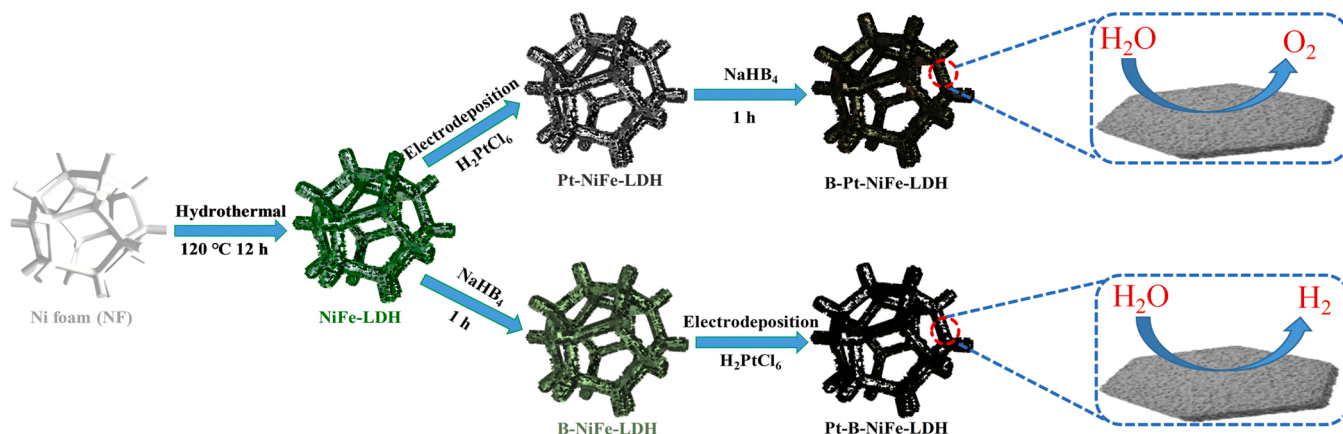


Fig. 1. Schematic representation of the preparation of B-Pt-NiFe-LDH and Pt-B-NiFe-LDH catalysts.

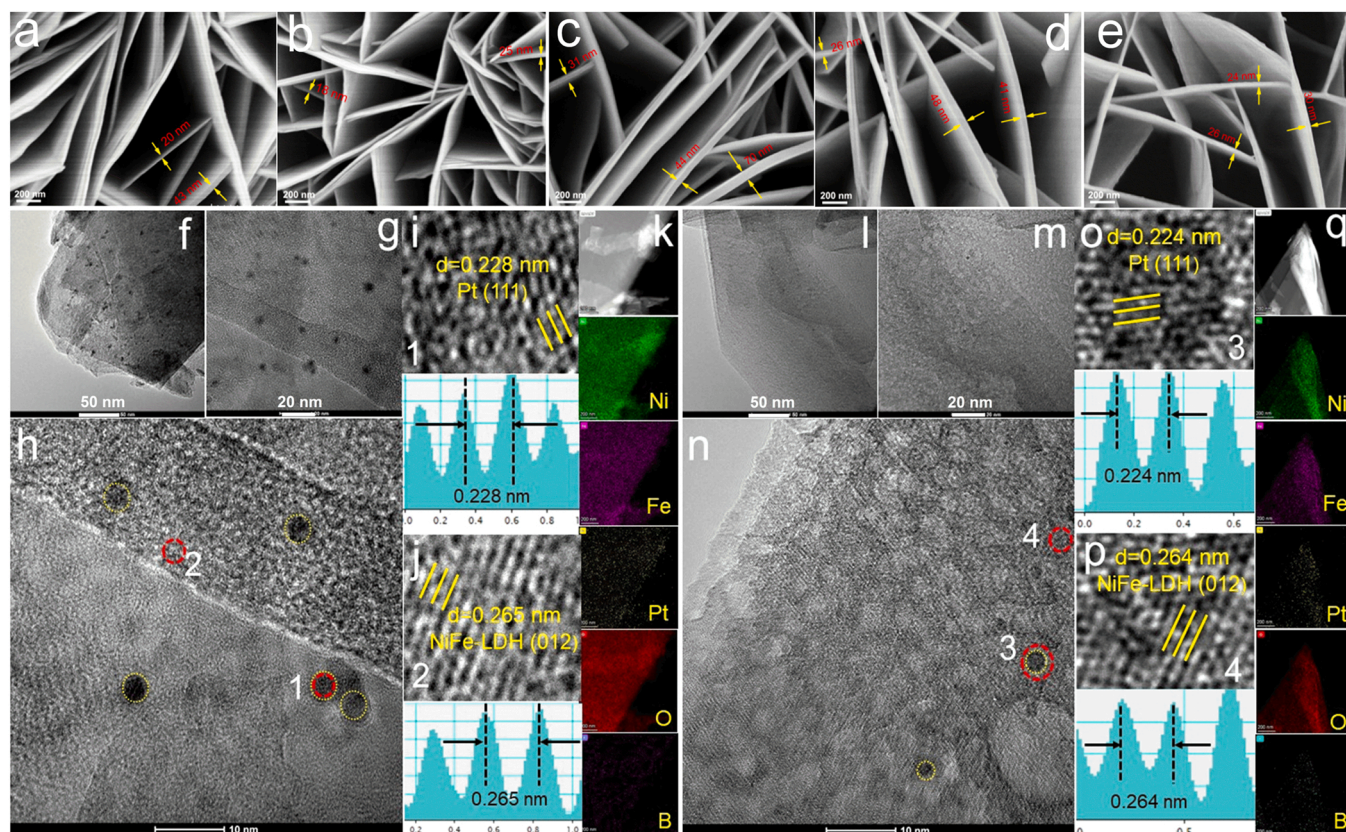


Fig. 2. SEM images of (a) NiFe-LDH, (b) B-NiFe-LDH, (c) Pt-NiFe-LDH, (d) B-Pt-NiFe-LDH, and (e) Pt-B-NiFe-LDH. (f-j) TEM and HRTEM of B-Pt-NiFe-LDH and (k) the TEM-EDS elemental mapping images of B-Pt-NiFe-LDH. (l-p) TEM and HRTEM of Pt-B-NiFe-LDH And (q) the TEM-EDS elemental mapping images of Pt-B-NiFe-LDH.

presence of corresponding elements in different catalysts. Their high-resolution spectra of Ni 2p subshells are shown in Fig. 3b. The featured sub-peaks at 855.8 eV and 873.3 eV originate from Ni^{2+} , while those at 857.3 eV and 874.80 eV stem from Ni^{3+} . For the Fe 2p spectra (Fig. 3c), the featured peaks at 707.5 eV and 723.4 eV correspond to Fe^{2+} , whereas those at 713.3 eV and 726.8 eV can be attributed to Fe^{3+} [65]. These sub-peak positions almost keep invariable, further verifying the stable LDH structure in all catalysts. The relative molar ratio of $\text{Ni}^{2+}/\text{Ni}^{3+}$ and $\text{Fe}^{2+}/\text{Fe}^{3+}$ experienced apparent change. Specifically, B-NiFe-LDH shows bigger $\text{Ni}^{2+}/\text{Ni}^{3+}$ and $\text{Fe}^{2+}/\text{Fe}^{3+}$ values (1.78 and 0.77, respectively) than NiFe-LDH (1.68 and 0.69, respectively) (Table S3 and S4), revealing that the reduction of NaBH_4 changed the electronic structure of metal sites. In addition, the increase of the +2 metallic forms suggests the electron transfer from B to NiFe-LDH and the strong interaction between both of them [66]. The deposition of Pt leads to an increased Ni^{3+} form in Pt-NiFe-LDH with a smaller $\text{Ni}^{2+}/\text{Ni}^{3+}$ value of 1.56, probably because the unstable high-valent Pt captured electrons from Ni [45]. The $\text{Fe}^{2+}/\text{Fe}^{3+}$ value of Pt-NiFe-LDH (0.68) is very close to that of NiFe-LDH, revealing that the Pt-deposition has negligible influence on Fe sites. The Pt 4f spectra of Pt-NiFe-LDH (Fig. 3d) display that its surface Pt species mainly occur in the oxidation state of Pt^{4+} (77.1 eV of Pt $4f_{5/2}$, and 73.7 eV of Pt $4f_{7/2}$) $\sim 38\%$ and Pt^{2+} (76.3 eV of Pt $4f_{5/2}$, and 71.6 eV of Pt $4f_{7/2}$) $\sim 62\%$ [67,68] (Table S5). For B-Pt-NiFe-LDH, the reductive role of NaBH_4 resulted in the absence of the Pt^{4+} peak and the synchronous appearance of Pt^{2+} (75.9 eV of Pt $4f_{5/2}$, and 72.4 eV of Pt $4f_{7/2}$) and Pt^0 (73.7 eV of Pt $4f_{5/2}$, and 70.8 eV of Pt $4f_{7/2}$) (Table S5), in which Pt^0 accounts for $\sim 82\%$. This reductive reaction also causes an increased Ni^{2+} portion in B-Pt-NiFe-LDH ($\text{Ni}^{2+}/\text{Ni}^{3+}$ is 1.69) (Table S3). The Pt species in Pt-B-NiFe-LDH is mainly present in low-valence with $\sim 66\%$ Pt^{2+} and $\sim 34\%$ Pt^0 but no Pt^{4+} because of the pre-introduction of B species. The increased Ni^{3+} and

Fe^{3+} percentages (Table S3 and S4) may be attributed to the oxidation of part metallic ions by the instantaneously formed high-valent Pt species. The B 1s spectra in Fig. S12b present the presence of Ni-B and Fe-B bands in very low contents in the three B-related catalysts. However, the Ni-B peaks in B-Pt-NiFe-LDH and Pt-B-NiFe-LDH display a clear positive shift compared with B-NiFe-LDH, indexing the strong electronic interaction between the Pt species and NiFe-LDH in both catalysts. The charge transfer and cation interaction in these catalysts are conducive to the appropriate electronic structure of metal sites for desirable OER or/and HER kinetics [5].

3.2. Electrocatalytic activity in 1M KOH

The OER activities of involved catalysts were performed in 1 M KOH solution with a conventional three-electrode configuration. Fig. 4a shows their LSV curves at a scan rate of 1 mV s^{-1} . Clearly, B-Pt-NiFe-LDH needs the smallest η_{100} (the overpotential at a current density of 100 mA cm^{-2}) of 208 mV compared to Pt-B-NiFe-LDH (229 mV), NiFe-LDH (279 mV), B-NiFe-LDH (240 mV), RuO_2 (261 mV), and Pt-NiFe-LDH (242 mV). This observation manifests that the formation of heterogeneous interfaces between Pt^0 species and NiFe-LDH is crucial to the enhancement of the OER activity. It should be noted that the predominant occurrence of Pt^0 species induced by the post-B-modification can tune the electronic structures of metallic sites of NiFe-LDH. Based on their corresponding Tafel plots in Fig. 4b, B-Pt-NiFe-LDH also reveals a lower Tafel slope of 30.4 mV dec^{-1} than Pt-B-NiFe-LDH (31.4 mV dec^{-1}), NiFe-LDH (69.4 mV dec^{-1}), B-NiFe-LDH (44.8 mV dec^{-1}), and Pt-NiFe-LDH (34.7 mV dec^{-1}), demonstrating its favorable affinity for oxygen species and fast OER kinetics [2]. The OER activity of B-Pt-NiFe-LDH outperforms many recently reported LDH-based catalysts (Table S6). The ECSA values of these electrocatalysts were determined

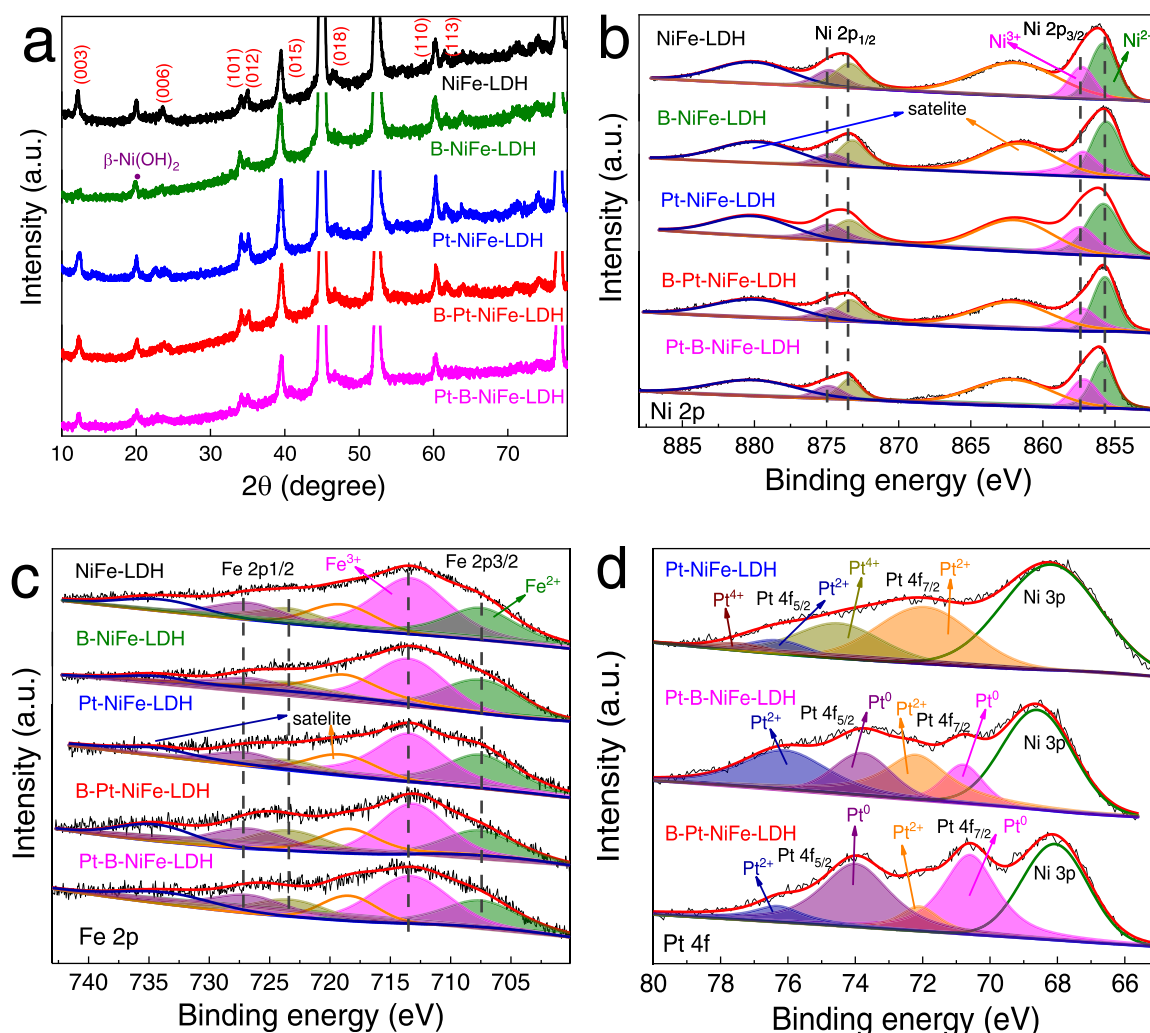


Fig. 3. (a) The XRD patterns of NiFe-LDH, B-NiFe-LDH, Pt-NiFe-LDH, B-Pt-NiFe-LDH, and Pt-B-NiFe-LDH. High-resolution XPS spectra of (b) Ni 2p, (c) Fe 2p, and (d) Pt 4f in NiFe-LDH, B-NiFe-LDH, Pt-NiFe-LDH, B-Pt-NiFe-LDH, and Pt-B-NiFe-LDH.

from their CV curves collected in the same non-faradaic zone at different scan rates [69]. The slopes of the fitted plots of the capacitive current density against the scan rate represent the corresponding doubled double-layer capacitance (C_{dl}) (Fig. 4c) based on CV curves (Fig. S13a-S13e). In the light of an equation: $ECSA = C_{dl}/C_s$ (the C_s was set as $40 \mu F cm^{-2}$) [70], the ECSA of B-Pt-NiFe-LDH was estimated to be $103.25 cm^{-2}$, which is higher than those for Pt-B-NiFe-LDH ($90.25 cm^{-2}$), NiFe-LDH ($29.25 cm^{-2}$), B-NiFe-LDH ($37.00 cm^{-2}$) and Pt-NiFe-LDH ($70.25 cm^{-2}$) (Fig. S13f). The largest ECSA is ascribed to the abundant interfaces between the Pt nanoclusters and NiFe-LDH. To further assess intrinsic activities, their area activities were calculated through normalization by ECSA (Fig. 4d). B-Pt-NiFe-LDH still exhibits the best area activity among these catalysts at higher potentials ($> \sim 1.43 V$ vs RHE), indicating outstanding inherent electrocatalytic activity to OER. The long-term stability of B-Pt-NiFe-LDH was evaluated by the chronopotentiometry technique as shown in Fig. 4e. This catalyst shows excellent stability as supported by only $\sim 10\%$ current loss after the continuous operation for 110 h at $50 mA cm^{-2}$. Fig. 4f depicts its multi-step chronoamperometry by changing applied potential to yield different current densities from 10 to $150 mA cm^{-2}$. B-Pt-NiFe-LDH almost instantaneously produces the current density peak and remains stable till to the end of each step, suggesting a low resistance for mass/charge transfer due to its special and stable nanostructure. The activity at the last step undergoes a tiny degradation during the 2 h operation, which could be attributed to the trace metal species dissolved at

$150 mA cm^{-2}$ during the OER [71,72]. After CV scanning for 2000 cycles, the potentials of B-Pt-NiFe-LDH at 50 and $100 mA cm^{-2}$ respectively took place positive shifts by 11 and 10 mV (Fig. S14), also offering validation for its good durability. The structural characteristics of B-Pt-NiFe-LDH after the abovementioned stability test were analyzed by different techniques. The B-Pt-NiFe-LDH catalyst keeps its original morphology and phase composition well (Figs. 5a, 5c, and Fig. S15). The Raman spectra (Fig. S16) evidence the new formation of metal (oxy) hydroxides at 477 and $554 cm^{-1}$, which are the real active centers for OER [73]. The peak positions in Ni 2p and Fe 2p spectra remain unchangeable (Figs. 5d-5e). The increased portion of high-valent metals (Ni^{2+}/Ni^{3+} and Fe^{2+}/Fe^{3+} are 1.46 and 0.53) means that some Ni and Fe species have evolved into Ni(Fe)-OOH during the OER test, which is in accord with the Raman results. In the Pt 4f spectra (Fig. 5f), although the Pt $4f_{5/2}$ peak positively shifts with an increased percentage of Pt^0 in Pt $4f_{5/2}$ due to the anodic process, the total Pt^0 proportion (71.7%) is almost equal to its initial value, indicating the stability of Pt^0 dispersed on LDH nanosheets (Table S9). The exceptional OER activity and durability can be ascribed to the unique heterostructure of B-Pt-NiFe-LDH. The deposited Pt species mainly in Pt^0 could optimize the adsorption energy of NiFe-LDH for oxygenated intermediates and the B-modification could strengthen the durability of the catalysts [46, 59].

The HER activities of all catalysts and Pt-NF were also determined under the alkaline condition and their LSV curves at a scan rate of

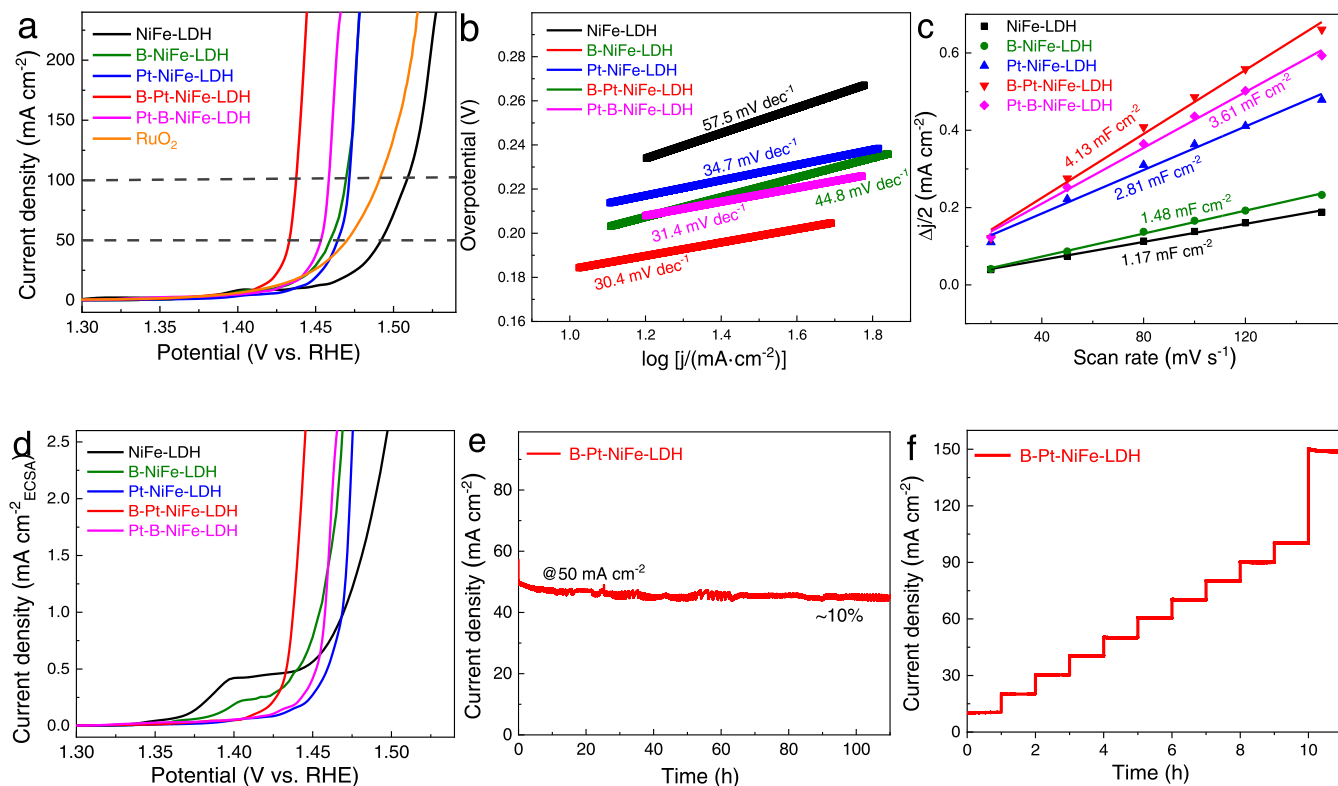


Fig. 4. LSV curves (a) and the corresponding Tafel plots (b) of NiFe-LDH, B-NiFe-LDH, Pt-NiFe-LDH, B-Pt-NiFe-LDH, RuO₂, and Pt-B-NiFe-LDH in 1.0 M KOH. The double-layer capacitances (C_{dl}) at 1.174 V (vs. RHE) (c) and their corresponding ECSA-normalized LSV curves (d). The chronoamperometric test of B-Pt-NiFe-LDH (e-f).

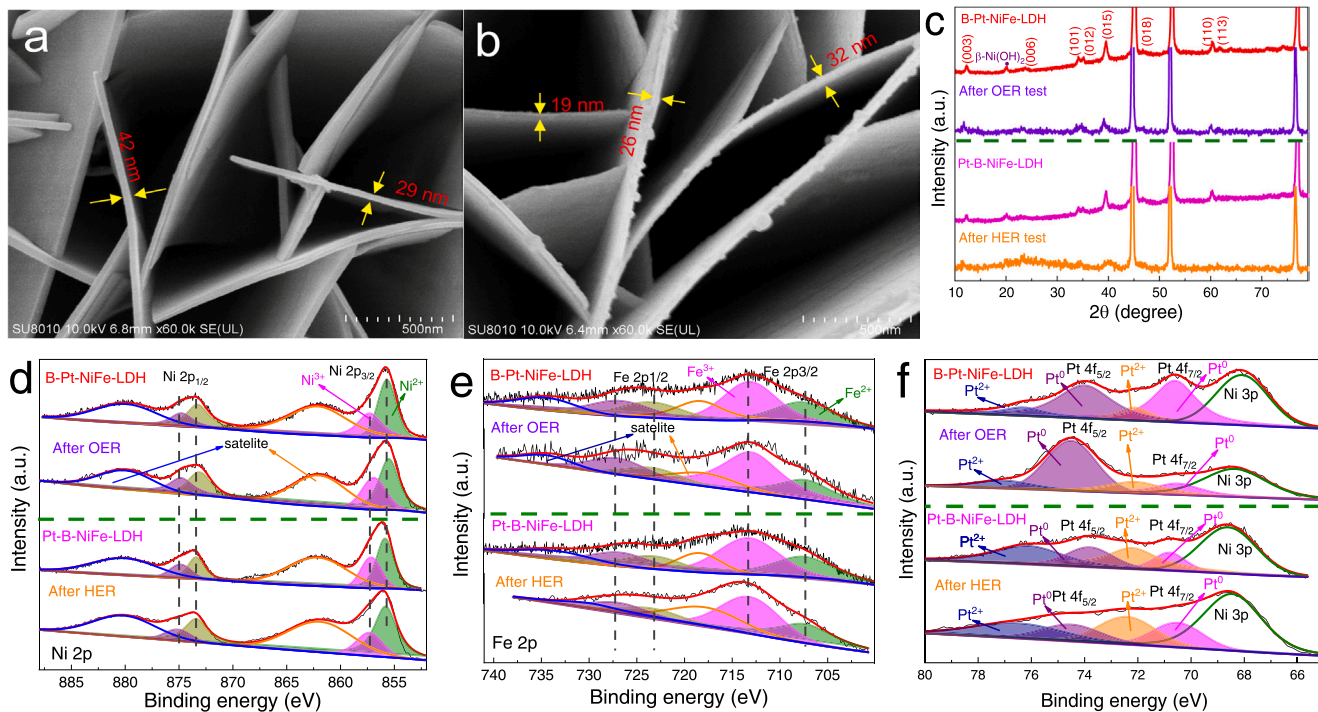


Fig. 5. SEM images of (a) B-Pt-NiFe-LDH after the OER test, and (b) Pt-B-NiFe-LDH after the HER test. (c) The XRD patterns of B-Pt-NiFe-LDH, Pt-B-NiFe-LDH, after the OER test, and after the HER test. High-resolution XPS spectra of (d) Ni 2p, (e) Fe 2p, and (f) Pt 4f in B-Pt-NiFe-LDH, Pt-B-NiFe-LDH, after OER test, and after HER test.

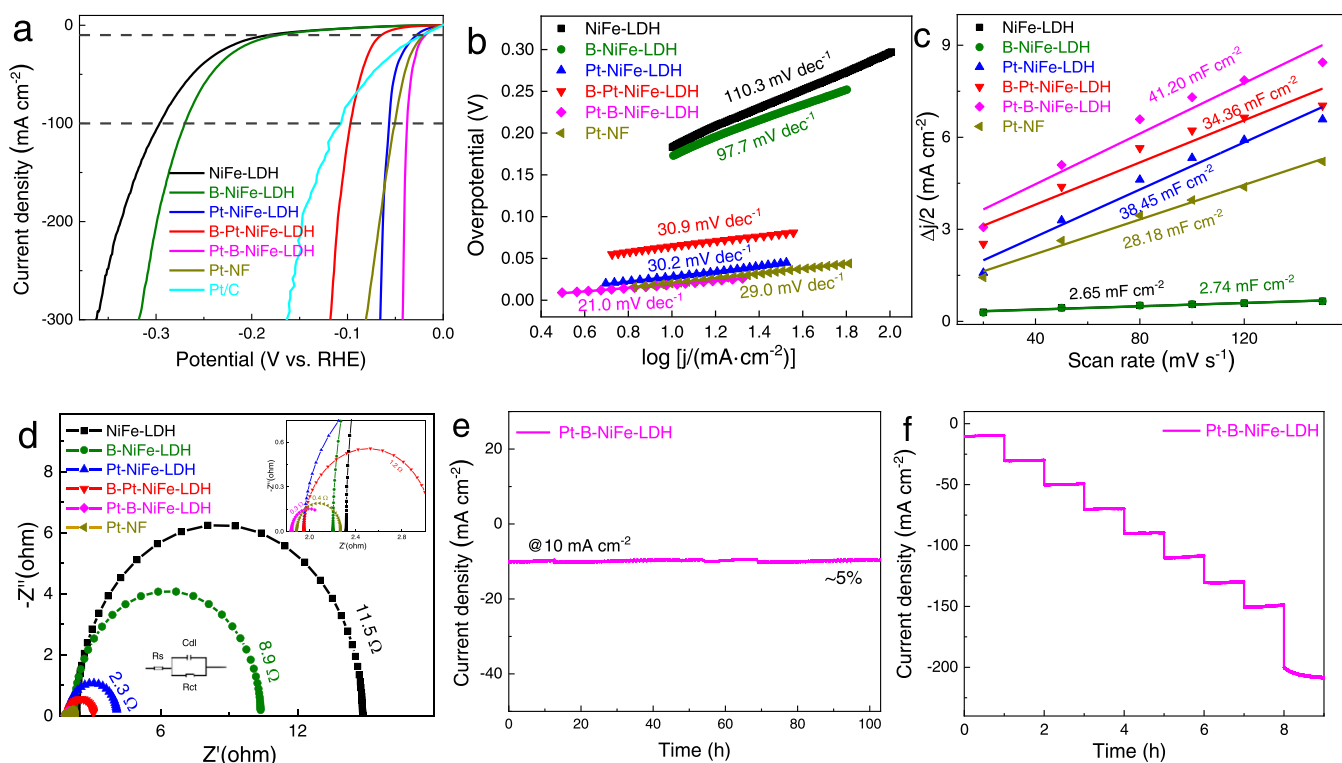


Fig. 6. (a) LSVs of NiFe-LDH, B-NiFe-LDH, Pt-NiFe-LDH, B-Pt-NiFe-LDH, Pt-B-NiFe-LDH, 20% Pt/C, and Pt-NF in 1.0 M KOH. (b) corresponding Tafel slopes. (c) C_{dl} at 0.074 V (vs. RHE). (d) Nyquist plots. and (e-f) the chronoamperometric and multistep chronoamperometric curves for Pt-B-NiFe-LDH.

5 mV s⁻¹ are presented in Fig. 6a. Differing from the OER case, Pt-B-NiFe-LDH performs the best HER activity among these catalysts. Specifically, the η_{10} and η_{100} values of the catalyst are respectively 19 and 38 mV, lower than those for Pt-NiFe-LDH (28 and 57 mV), Pt-NF (21 and 51 mV), Pt/C (22 and 107 mV), and B-Pt-NiFe-LDH (65 and 97 mV), but drastically lower than those for B-NiFe-LDH (173 and 270 mV) and NiFe-LDH (183 and 296 mV). It is noticeable that the Pt-based samples are far superior to the non-Pt ones, strongly hinting that the Pt species is the real HER active phase. For these Pt-based products, their HER activities appear in the order of Pt-B-NiFe-LDH > Pt-NF > Pt-NiFe-LDH > B-Pt-NiFe-LDH probably because of the different electronic properties of the Pt species induced by various coordination environments in the individual catalyst. In detail, although Pt-B-NiFe-LDH and B-Pt-NiFe-LDH have both Pt²⁺ and Pt⁰ forms, the former has far more Pt²⁺ (~66%) than the latter (~18%). Pt-NiFe-LDH displays two oxidized Pt forms of Pt²⁺ (~62%) and Pt⁴⁺ (~38%). It was declared that the HER activity of Pt species increases initially upon increasing its oxidation state since Pt in a high oxidation state can afford more favorable adsorption for H₂O, OH*, and H*. However, too strong H* adsorption will, in turn, retard the release of active sites and lower the HER kinetics. The Pt species in + 2 possesses moderate Pt-H interaction to release H₂ and Pt-OH interaction to split H₂O, thus greatly boosting the overall alkaline HER activity [74]. The second-best HER activity of Pt-NF is due to its higher Pt-loading (0.496 mg cm⁻²) than the others (Table S2), however, this catalyst exhibits a largely inferior HER mass activity to the others (Fig. S18a). The above fundamental conclusion strongly supported our finding that the HER activity of Pt-B-NiFe-LDH is superior to Pt-NiFe-LDH and B-Pt-NiFe-LDH in sequence. The η_{10} value of Pt-B-NiFe-LDH is comparable to or better than those of other reported Pt-based HER catalysts such as NF-Na-Fe-Pt (31 mV), N, Pt-MoS₂ (38 mV), Pt_{5A}/α-MoC_{1-x}@C-0.75 (21 mV), and others in 1 M KOH (Table S10). Its η_{100} value is even on par with the reported Pt/C catalysts [75,76]. As illustrated in Fig. 6b, Pt-B-NiFe-LDH also shows a lower Tafel slope of 21.0 mV dec⁻¹ than those for NiFe-LDH (110.3 mV dec⁻¹),

B-NiFe-LDH (97.7 mV dec⁻¹), Pt-NiFe-LDH (30.2 mV dec⁻¹), B-Pt-NiFe-LDH (30.9 mV dec⁻¹), and Pt/NF (29.0 mV dec⁻¹), revealing a favorable HER kinetics for this catalyst. According to the C_{dl} values derived from their CV curves (Fig. 6c and Fig. S17), the ECSA of Pt-B-NiFe-LDH was estimated to be 1030 cm², which is distinctly larger than those for Pt-NF (704.5 cm²), Pt-NiFe-LDH (961.3 cm²), and B-Pt-NiFe-LDH (869.5 cm²), but is almost 15 times of those for non-Pt catalysts of NiFe-LDH (66.3 mF cm⁻²) and B-NiFe-LDH (68.5 mF cm⁻²). The mass activity (Fig. S18a) and ECSA-normalized data (Fig. S18b) also exhibit the same sequence as those in Figs. 6a and 6b. EIS analysis was scrutinized to acquire further insight into their intrinsic HER electrocatalytic kinetics. Fig. 6d displays the charge-transfer resistance (R_{ct}) value of Pt-B-NiFe-LDH was measured to be ~0.3 Ω, slightly smaller than those of Pt-NF (~0.4 Ω), B-Pt-NiFe-LDH (~1.2 Ω) and Pt-NiFe-LDH (~2.3 Ω), but largely lower than those of NiFe-LDH (~11.5 Ω) and B-NiFe-LDH (~8.9 Ω). Therefore, it can be inferred that Pt-B-NiFe-LDH has a fast charge transfer and HER kinetics in alkaline electrolytes [77]. The HER durability of the catalyst electrode was also tested by chronoamperometry. As depicted in Fig. 6e, the current density gives rise to merely less than a 5% reduction after operation over 100 h at η_{10} . The multi-step chronoamperometry implies a quick response and stable running in each step at different overpotentials from η_{10} to η_{200} (Fig. 6f). The LSV curve of Pt-B-NiFe-LDH decreased by 6 and 21 mV at current densities of 10 and 100 mA cm⁻², respectively, after 2000 CV cycles (Fig. S19). Hence, it is suggested that Pt-B-NiFe-LDH performs excellent long-term stability. Its structural stability was also assessed by analyzing the catalyst after the HER test. As shown in SEM images (Fig. 5b and Fig. S20), some Pt nanoparticles in 10–70 nm formed on the NiFe-LDH sheets after the HER stability test since the Pt species mainly in Pt⁰ agglomerated accompanying the generation of more Pt⁰ form in such reductive environment. This phase transformation and the aggregation of Pt nanoclusters could be responsible for the HER performance loss after 2000 CV cycles. The XRD patterns (Fig. 5c) and Raman spectra (Fig. S16) suggest that the structural position of Pt-B-NiFe-LDH

remained well after the HER stability test. The XPS spectra of Pt 4f (Fig. 5f) demonstrate a slight decrease in Pt^{2+} percentage ($\sim 57\%$) compared with the initial catalyst ($\sim 66\%$). The peaks of Ni 2p and Fe 2p remain unchanged (Figs. 5d and 5e), but the $\text{Ni}^{2+}/\text{Ni}^{3+}$ value greatly increases from an initial 1.66–2.55 due to the reductive HER process. The excellent HER catalytic activity and durability could be assigned to the special heterostructure of Pt-B-NiFe-LDH. The defect-rich B-modified NiFe-LDH could confine the Pt species mainly in Pt^{2+} to offer plentiful water adsorption/dissociation sites and regulate the electronic structure of Pt. As such, B-modified NiFe-LDH is employed to break the H–OH bond and Pt to promote HER [78,79].

Intrigued by their remarkable HER and OER performances, an alkaline electrolyzer was assembled by respectively employing B-Pt-NiFe-LDH and Pt-B-NiFe-LDH as the anode and cathode of the overall water-splitting system (B-Pt-NiFe-LDH//Pt-B-NiFe-LDH) in 1 M KOH solution. As shown in Fig. 7a, the B-Pt-NiFe-LDH//Pt-B-NiFe-LDH electrolyzer only needed an extraordinarily low cell voltage of 1.475 V to deliver a current density of 10 mA cm^{-2} , which was lower than most of the reported water splitting catalysts (Table S11). In addition, at the voltage of 1.6 V, the current density reaches $\sim 311 \text{ mA cm}^{-2}$, which is about 9 times the RuO_2 //Pt/C cell using NF supporting RuO_2 and Pt/C as electrodes. This overall water-splitting configuration demonstrates good durability as convinced by its stable operation over 110 h (Fig. 7b). After the above stability test, no Pt element was detected in the electrolyte by ICP, indicating that almost no Pt species was dissolved from the two electrodes by the electrolyte. The faradaic efficiency (FE) of the electrolyzer was evaluated using chronoamperometry in 1 M KOH solution at room temperature by a drainage method (Fig. S21). As shown in Fig. 7c, the measured volume of O_2 and H_2 matched well with the theoretical amount of them and the corresponding FE is about 99%.

Furthermore, the density functional theory (DFT) calculations were implemented to unravel the possible origin for the preeminent performances of B-Pt-NiFe-LDH toward OER and Pt-B-NiFe-LDH toward HER. It should be noted that, in the two catalysts, the B-modification principally contributes to the catalytic performances by amorphizing the LDH nanosheets' surfaces and modulating the electronic states of the interfacial Pt species. Besides, the B content was detected to be nearly close to zero in the two catalysts by ICP. Therefore, we built two theoretical models only by incorporating the Pt species in different states into NiFe-LDH nanosheets without considering the B element (Fig. S22). According to the detailed valances of the Pt species in catalysts, the B-Pt-NiFe-LDH and Pt-B-NiFe-LDH were respectively denoted as Pt^0 -NiFe-LDH and $\text{Pt}^{2+/4+}$ -NiFe-LDH for easier understanding in the DFT calculation part. The charge density differences of the two catalysts are illustrated in Fig. 8a. It can be observed the significant charge redistributions at the Pt-OH bonding regions, which is probably responsible for the enhanced catalytic activities. For Pt^0 -NiFe-LDH, owing to the bigger electronegativity of O (3.44) than Pt (2.28), electron density accumulates around O sites of NiFe-LDH and depletes around the Pt atoms neighboring O

species. Whereas, the Pt atom far away from LDH is still in an electron-rich state because it can keep its metallic state by capturing electrons from the near Pt atoms. For $\text{Pt}^{2+/4+}$ -NiFe-LDH, the Pt species exhibits the oxidative state due to the electron transfer from Pt to the O sites in both NiFe-LDH and Pt-O_x . The calculated density of states (DOS) in Fig. 8b reveals that the d-band center (E_d) energy levels of Pt^0 -NiFe-LDH (-2.535 eV) and $\text{Pt}^{2+/4+}$ -NiFe-LDH (-2.343 eV) are higher than that of NiFe-LDH (-3.048 eV), indicating that the E_d values are closer to the Fermi level (E_f) [80]. This fact suggests that the Pt species in either metallic or oxidative state can improve the electrical conductivity of NiFe-LDH [81]. The 4-electron OER pathway over Pt^0 -NiFe-LDH, $\text{Pt}^{2+/4+}$ -NiFe-LDH, and NiFe-LDH was illustrated in Fig. S23–S27. The LDH site and Pt site were chosen as active sites to investigate their OER process and their Gibbs free energy (ΔG) diagrams are shown in Fig. 8c. The rate-determining step (RDS) during OER is the oxidation of *O to *OOH on all three catalysts [82]. The ΔG values on the Pt site are much larger than those on the LDH site, revealing that Pt is not an active site for OER but a co-catalyst of NiFe-LDH. The ΔG of RDS for Pt^0 -NiFe-LDH (1.647 eV) is lower than those for $\text{Pt}^{2+/4+}$ -NiFe-LDH (1.872 eV), and NiFe-LDH (2.076 eV) on LDH site at $U = 0 \text{ V}$ (Fig. 8c), suggesting that the metallic Pt (Pt^0) anchored on NiFe-LDH is more conducive to improving OER activity. The Gibbs free energy of H^* intermediate adsorption (ΔG_{H^*}) is a critical parameter for the prediction of the HER activity. The H^* adsorption models on the three catalysts by Pt and LDH sites are shown in Fig. S28–S32 and the corresponding ΔG_{H^*} values were calculated as shown in Fig. 8d. The ΔG_{H^*} values of $\text{Pt}^{2+/4+}$ -NiFe-LDH and Pt^0 -NiFe-LDH by the LDH site are respectively -1.524 and -1.209 eV , much closer to 0 eV compared to NiFe-LDH (-1.658 eV), disclosing that the difficult H_2 evolution on NiFe-LDH due to its strong bind for H^* intermediates can be mitigated by incorporating Pt species. Impressively, on the Pt site, $\text{Pt}^{2+/4+}$ -NiFe-LDH delivers the ΔG_{H^*} value (-0.235 eV) closer to zero than Pt^0 -NiFe-LDH (-0.514 eV), demonstrating that the $\text{Pt}^{2+/4+}$ form decorated on NiFe-LDH is more favorable for quick HER than the metallic Pt. It is known that water-splitting involves water dissociation and the H-coupling to H_2 , which are dependent on how H_2O , OH , and H bond to the active sites on the catalyst's surface [83]. As shown in Fig. S33, the NiFe-LDH site in Pt^0 -NiFe-LDH showcases stronger adsorption for both H_2O and OH than the Pt site, indicating the NiFe-LDH layer is beneficial for rapid water dissociation. However, the adsorption energies for H manifest that the H atoms absorbed on NiFe-LDH are difficult to desorb, thus they have to transfer to the nearby Pt nanocluster (Pt^0) surface and are then converted into H_2 . For $\text{Pt}^{2+/4+}$ -NiFe-LDH, the Pt site shows a preference for stabilizing H_2O and OH over the NiFe-LDH site due to the linkage of the OH groups in LDH with the oxidized Pt species. It can be inferred that the dissociation of H_2O occurs on the Pt-OH interface between the Pt species and the LDH sheets. The dissociated H atoms are attached preferentially to Pt sites, which shortened the distance of HER but extended the distance of OH adsorption. Therefore, $\text{Pt}^{2+/4+}$ -NiFe-LDH and Pt^0 -NiFe-LDH display

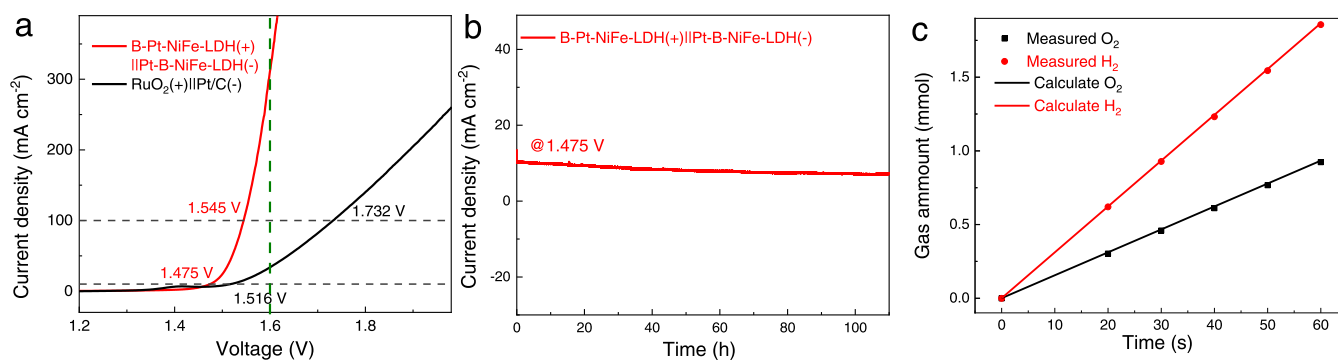


Fig. 7. (a) LSV curves of the B-Pt-NiFe-LDH//Pt-B-NiFe-LDH electrolyzer in 1 M KOH. (b) Chronopotentiometric curve of water splitting for this electrolyzer at 10 mA cm^{-2} for over 110 h. (c) Measured and theoretical gaseous products from B-Pt-NiFe-LDH//Pt-B-NiFe-LDH electrolyzer at 100 mA cm^{-2} in 1 M KOH.

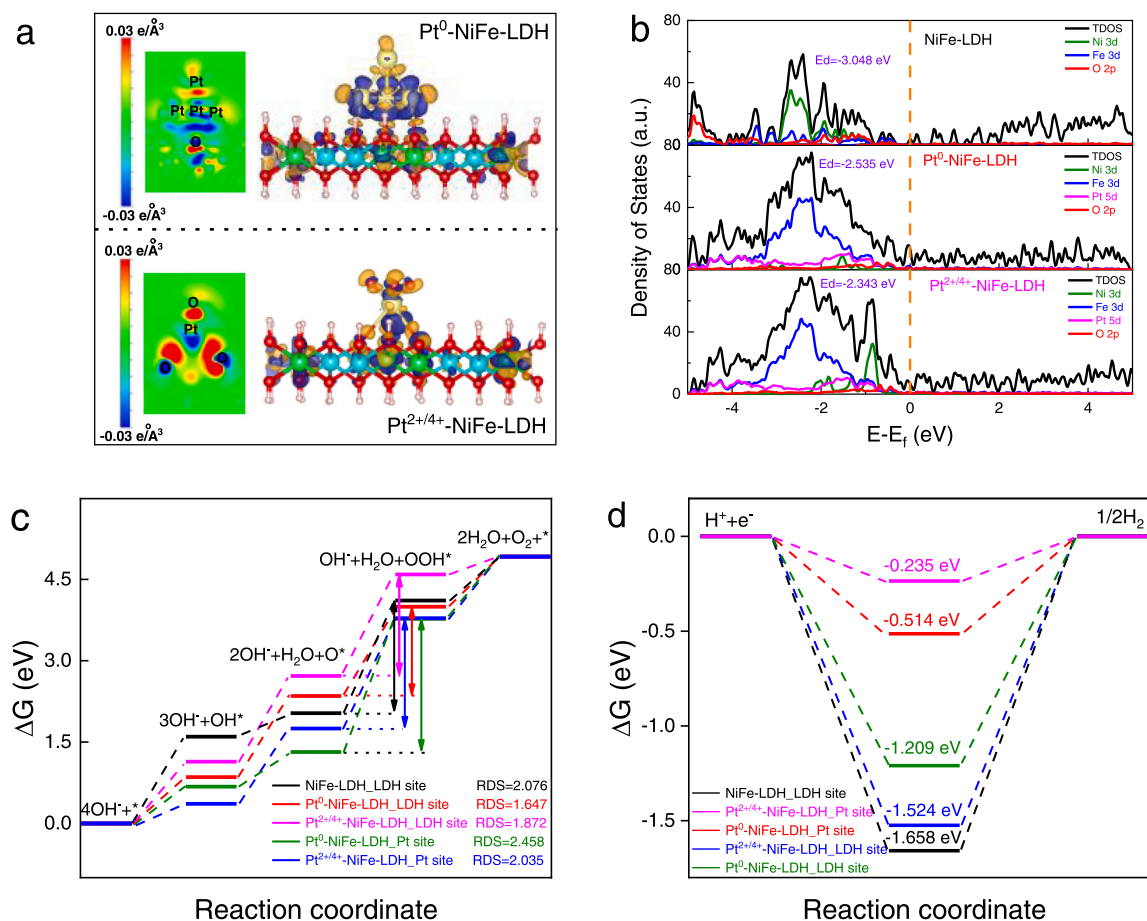


Fig. 8. (a) Differential charge density of Pt⁰-NiFe-LDH (top) and Pt^{2+/4+}-NiFe-LDH (down) (orange and dark blue contours represent the charge accumulation and depletion, respectively) (green: Fe, blue: Ni, red: O, white: H). (b) The density of states (DOS) on NiFe-LDH, Pt⁰-NiFe-LDH, and Pt^{2+/4+}-NiFe-LDH. (c, d) The calculated free energy diagrams (ΔG) for the OER and HER of NiFe-LDH, Pt⁰-NiFe-LDH, and Pt^{2+/4+}-NiFe-LDH at U = 0.

better HER and OER performance than the others, respectively.

4. Conclusions

In summary, we report the synthesis of two electrocatalysts of B-Pt-NiFe-LDH and Pt-B-NiFe-LDH by combining the boron-modification and Pt-deposition in various orders with low Pt contents (0.781 wt% for B-Pt-NiFe-LDH and 1.019 wt% for Pt-B-NiFe-LDH). B-Pt-NiFe-LDH displays superior alkaline OER performance due to active NiFe-LDH sites and the heterogeneous interface between the Pt⁰ species and LDH. Pt-B-NiFe-LDH shows superior alkaline HER performance owing to active Pt²⁺ species assembled on the co-catalyst of B-modified NiFe-LDH. The corresponding electrolyzer of B-Pt-NiFe-LDH//Pt-B-NiFe-LDH only requires a very low voltage of 1.475 V to deliver 10 mA cm⁻² with good durability which is much better than that of the RuO₂//Pt/C cell (1.516 V). DFT results demonstrate that the inherently poor conductivity of NiFe-LDH is improved in the two catalysts. The introduction of the Pt⁰ species on NiFe-LDH in B-Pt-NiFe-LDH lowers the energy barrier of OER, while the decoration of the Pt^{2+/4+} components on NiFe-LDH in Pt-B-NiFe-LDH can stabilize H₂O and OH but makes H-desorption easier, which thus causes a ΔG_{H^*} value (-0.235 eV) closest to 0 that improve HER performance. This work demonstrates the rational strategy to fabricate high-performance electrocatalysts for water-splitting.

CRediT authorship contribution statement

Lei Tan: Investigation, Methodology, Data curation, Software, Writing – original draft. **Haifeng Wang:** Data curation, Writing –

original draft. **Chunhong Qi:** Data curation, Software, Investigation. **Xuan Peng:** Data curation, Investigation. **Xiangxiang Pan:** Investigation. **Xiaotong Wu:** Investigation. **Zekun Wang:** Investigation. **Lin Ye:** Investigation. **Qi Xiao:** Writing – review & editing. **Wei Luo:** Validation, Supervision. **Hongtao Gao:** Validation, Supervision. **Wanguo Hou:** Validation, Supervision. **Xiaopeng Li:** Validation, Supervision. **Tianrong Zhan:** Methodology, Project administration, Writing – review & editing.

Declaration of Competing Interest

The authors declare that they have no known competing financial interests or personal relationships that could have appeared to influence the work reported in this paper.

Data availability

Data will be made available on request.

Acknowledgments

This work is financially supported by the Natural Science Foundation of Shandong Province, China (No. ZR2019MB062 and ZR2014JL013), the Key Research and Development Program of Shandong Province (2017GGX20143), the Foundation of Key Laboratory of Sensor Analysis of Tumor Marker, Ministry of Education, QUST (SATM201603), and the foundation of Key Laboratory of Colloid and Interface Chemistry (Shandong University), the Foundation of Division of Chemical Sciences

of Qingdao University of Science and Technology (No. QUSTHX201810), Ministry of Education (201702).

Appendix A. Supporting information

Supplementary data associated with this article can be found in the online version at [doi:10.1016/j.apcatb.2023.123352](https://doi.org/10.1016/j.apcatb.2023.123352).

References

- [1] J. Hwang, R. Rao, L. Giordano, Y. Katayama, Y. Yu, Y. Shao-Horn, Perovskites in catalysis and electrocatalysis, *Science* 358 (2017) 751–756, <https://doi.org/10.1126/science.aam7092>.
- [2] Y. Jiao, Y. Zheng, M. Jaroniec, S. Qiao, Design of electrocatalysts for oxygen- and hydrogen-involving energy conversion reactions, *Chem. Soc. Rev.* 44 (2015) 2060–2086, <https://doi.org/10.1039/C4CS00470A>.
- [3] Y. Jin, H. Wang, J. Li, X. Yue, Y. Han, P.K. Shen, Y. Cui, Porous MoO₂ nanosheets as non-noble bifunctional electrocatalysts for overall water splitting, *Adv. Mater.* 28 (2016) 3785–3790, <https://doi.org/10.1002/adma.201506314>.
- [4] L. Hui, Y. Xue, B. Huang, H. Yu, C. Zhang, D. Zhang, D. Jia, Y. Zhao, Y. Li, H. Liu, Y. Li, Overall water splitting by graphdiyne-exfoliated and -sandwiched layered double-hydroxide nanosheet arrays, *Nat. Commun.* 9 (2018) 5309, <https://doi.org/10.1038/s41467-018-07790-x>.
- [5] A. Li, Z. Zhang, J. Feng, F. Lv, Y. Li, R. Wang, M. Lu, R.B. Gupta, P. Xi, S. Zhang, Heterostructure-promoted oxygen electrocatalysis enables rechargeable zinc-air battery with neutral aqueous electrolyte, *J. Am. Chem. Soc.* 140 (2018) 17624–17631, <https://doi.org/10.1021/jacs.8b09805>.
- [6] L. Tan, J. Yu, C. Wang, H. Wang, X. Liu, H. Gao, L. Xin, D. Liu, W. Hou, T. Zhan, Partial sulfidation strategy to NiFe-LDH@FeNi₂S₄ heterostructure enable high-performance water/seawater oxidation, *Adv. Funct. Mater.* 32 (2022) 2200951, <https://doi.org/10.1002/adfm.202200951>.
- [7] H. Wang, S. Xu, C. Tsai, Y. Li, C. Liu, J. Zhao, Y. Liu, H. Yuan, F. Abild-Pedersen, F. B. Prinz, J.K. Nørskov, Y. Cui, Direct and continuous strain control of catalysts with tunable battery electrode, *Mater. Sci.* 354 (2016) 1031–1036, <https://doi.org/10.1126/science.aaf7680>.
- [8] M. Escudero-Escribano, P. Malacrida, M.H. Hansen, U.G. Vej-Hansen, A. Velazquez-Palenzuela, V. Tripkovic, J. Schiotz, J. Rossmeisl, I.E. Stephens, I. Chorkendorff, Tuning the activity of Pt alloy electrocatalysts by means of the lanthanide contraction, *Science* 352 (2016) 73–76, <https://doi.org/10.1126/science.aad8892>.
- [9] X. Li, Y. Sun, Q. Wu, H. Liu, W. Gu, X. Wang, Z. Cheng, Z. Fu, Y. Lu, Optimized electronic configuration to improve the surface absorption and bulk conductivity for enhanced oxygen evolution reaction, *J. Am. Chem. Soc.* 141 (2019) 3121–3128, <https://doi.org/10.1021/jacs.8b12299>.
- [10] F. Garcés-Pineda, M. Blasco-Ahicart, D. Nieto-Castro, N. Lopez, J. Galan-Mascaros, Direct magnetic enhancement of electrocatalytic water oxidation in alkaline media, *Nat. Energy* 4 (2019) 519–525, <https://doi.org/10.1038/s41560-019-0404-4>.
- [11] L. Seitz, C. Dickens, K. Nishio, Y. Hikita, J. Montoya, A. Doyle, C. Kirk, A. Vojvodic, H. Hwang, J. Nørskov, T. Jaramillo, A highly active and stable IrO₃/SrIrO₃ catalyst for the oxygen evolution reaction, *Science* 353 (2016) 1011–1014, <https://doi.org/10.1126/science.aaf5050>.
- [12] J. Chen, P. Cui, G. Zhao, K. Rui, M. Lao, Y. Chen, X. Zheng, Y. Jiang, H. Pan, S. X. Dou, W. Sun, Low-coordinate iridium oxide confined on graphitic carbon nitride for highly efficient oxygen, *Evol. Angew. Chem. Int. Ed.* 58 (2019) 12540–12544, <https://doi.org/10.1002/anie.201907017>.
- [13] L. Zeng, Z. Zhao, F. Lv, Z. Xia, S. Lu, J. Li, K. Sun, K. Wang, Y. Sun, Q. Huang, Y. Chen, Q. Zhang, L. Gu, G. Lu, S. Guo, Anti-dissolution Pt single site with Pt(OH)(O₃)/Co(P) coordination for efficient alkaline water splitting electrolyzer, *Nat. Commun.* 13 (2022) 3822, <https://doi.org/10.1038/s41467-022-31406-0>.
- [14] X. Zheng, P. Cui, Y. Qian, G. Zhao, X. Zheng, X. Xu, Z. Cheng, Y. Liu, S. Dou, W. Sun, Multifunctional active-center-transferable platinum/lithium cobalt oxide heterostructured electrocatalysts towards superior water splitting, *Angew. Chem. Int. Ed.* 59 (2020) 14533–14540, <https://doi.org/10.1002/anie.202005241>.
- [15] Y. Wu, W. Wei, R. Yu, L. Xia, X. Hong, J. Zhu, J. Li, L. Lv, W. Chen, Y. Zhao, L. Zhou, L. Mai, Anchoring sub-nanometer Pt clusters on crumpled paper-like MXene enables high hydrogen evolution mass activity, *Adv. Funct. Mater.* 32 (2022) 2110910, <https://doi.org/10.1002/adfm.202110910>.
- [16] A. Geim, I. Grigorieva, Van der Waals heterostructures, *Nature* 499 (2013) 419–425, <https://doi.org/10.1038/nature12385>.
- [17] Z. Liu, J. Qi, M. Liu, S. Zhang, Q. Fan, H. Liu, K. Liu, H. Zheng, Y. Yin, C. Gao, Aqueous synthesis of ultrathin platinum/non-noble metal alloy nanowires for enhanced hydrogen evolution activity, *Angew. Chem. Int. Ed.* 57 (2018) 11678–11682, <https://doi.org/10.1002/anie.201806194>.
- [18] Y. Chen, G. Zhao, W. Sun, Strategies of engineering 2D nanomaterial-based electrocatalysts toward hydrogen evolution reaction, *Mater. Renew. Sustain. Energy* 9 (2020) 10, <https://doi.org/10.1007/s40243-020-00170-w>.
- [19] L. Dai, Z.N. Chen, L. Li, P. Yin, Z. Liu, H. Zhang, Ultrathin Ni(OH)₂-embedded Ni(OH)₂ heterostructured nanosheets with enhanced electrochemical overall water splitting, *Adv. Mater.* 32 (2020) 1906915, <https://doi.org/10.1002/adma.201906915>.
- [20] W. Jiang, L. Gu, L. Li, Y. Zhang, X. Zhang, L. Zhang, J. Wang, J. Hu, Z. Wei, L. Wan, Understanding the high activity of Fe–N–C electrocatalysts in oxygen reduction: Fe/Fe₃C nanoparticles boost the activity of Fe–N_x, *J. Am. Chem. Soc.* 138 (2016) 3570–3578, <https://doi.org/10.1021/jacs.6b00757>.
- [21] S. Yang, J. Zhu, X. Chen, M. Huang, S. Cai, J. Han, J. Li, Self-supported bimetallic phosphides with artificial heterointerfaces for enhanced electrochemical water splitting, *Appl. Catal. B* 304 (2022), 120914, <https://doi.org/10.1016/j.apcatb.2021.120914>.
- [22] G. Zhao, P. Li, N. Cheng, S.X. Dou, W. Sun, An Ir/Ni(OH)₂ heterostructured electrocatalyst for the oxygen evolution reaction: breaking the scaling relation, stabilizing iridium(V), and beyond, *Adv. Mater.* 32 (2020) 2000872, <https://doi.org/10.1002/adma.202000872>.
- [23] J. Ng, M. García-Melchor, M. Bajdich, P. Chakthranont, C. Kirk, A. Vojvodic, T. Jaramillo, Gold-supported Cerium-doped NiO_x catalysts for water oxidation, *Nat. Energy* 1 (2016) 16053, <https://doi.org/10.1038/nenergy.2016.53>.
- [24] Q. Han, Y. Luo, J. Li, X. Du, S. Sun, Y. Wang, G. Liu, Z. Chen, Efficient NiFe-based oxygen evolution electrocatalysts and origin of their distinct activity, *Appl. Catal. B* 304 (2022), 120937, <https://doi.org/10.1016/j.apcatb.2021.120937>.
- [25] T. He, W. Wang, F. Shi, X. Yang, X. Li, J. Wu, Y. Yin, M. Jin, Mastering the surface strain of platinum catalysts for efficient electrocatalysis, *Nature* 598 (2021) 76–81, <https://doi.org/10.1038/s41586-021-03870-z>.
- [26] K. Jiang, B. Liu, M. Luo, S. Ning, M. Peng, Y. Zhao, Y. Lu, T. Chan, F. Groot, Y. Tan, Single platinum atoms embedded in nanoporous cobalt selenide as electrocatalyst for accelerating hydrogen evolution reaction, *Nat. Commun.* 10 (2019) 1743, <https://doi.org/10.1038/s41467-019-09765-y>.
- [27] Q. Xue, X. Bai, Y. Zhao, Y. Li, T. Wang, H. Sun, F. Li, P. Chen, P. Jin, S. Jin, Y. Chen, Au core-PtAu alloy shell nanowires for formic acid electrolysis, *J. Energy Chem.* 65 (2022) 94–102, <https://doi.org/10.1016/j.jecchem.2021.05.034>.
- [28] Y. Ding, K. Cao, J. He, F. Li, H. Huang, P. Chen, Y. Chen, Nitrogen-doped graphene aerogel-supported ruthenium nanocrystals for pH-universal hydrogen evolution reaction, *Chinese, J. Catal.* 43 (2022) 1535–1543, [https://doi.org/10.1016/S1872-6627\(21\)63977-3](https://doi.org/10.1016/S1872-6627(21)63977-3).
- [29] R. Gao, J. Wang, Z. Huang, R. Zhang, W. Wang, L. Pan, J. Zhang, W. Zhu, X. Zhang, C. Shi, J. Lim, J. Zou, Pt/Fe₃O₄ with Pt–Fe pair sites as a catalyst for oxygen reduction with ultralow Pt loading, *Nat. Energy* 6 (2021) 614–623, <https://doi.org/10.1038/s41560-021-00826-5>.
- [30] Z. Seh, J. Kibsgaard, C. Dickens, I. Chorkendorff, J. Nørskov, T. Jaramillo, Combining theory and experiment in electrocatalysis: insights into materials design, *Science* 355 (2017) 6321, <https://doi.org/10.1126/science.aad4998>.
- [31] R. Arrigo, M. Havecker, M. Schuster, C. Ranjan, E. Stotz, A. Knop-Gericke, R. Schlögl, In situ study of the gas-phase electrolysis of water on platinum by NAP-XPS, *Angew. Chem. Int. Ed.* 52 (2013) 11660–11664, <https://doi.org/10.1002/anie.201304765>.
- [32] H. Fei, J. Dong, Y. Feng, C. Allen, C. Wan, B. Voloskiy, M. Li, Z. Zhao, Y. Wang, H. Sun, P. An, W. Chen, Z. Guo, C. Lee, D. Chen, I. Shakir, M. Liu, T. Hu, Y. Li, A. Kirkland, X. Duan, Y. Huang, General synthesis and definitive structural identification of MN₄C₄ single-atom catalysts with tunable electrocatalytic activities, *Nat. Catal.* 1 (2018) 63–72, <https://doi.org/10.1038/s41929-017-0008-y>.
- [33] H. Lei, L. Ma, Q. Wan, S. Tan, B. Yang, Z. Wang, W. Mai, H. Fan, Promoting surface reconstruction of NiFe layered double hydroxide for enhanced oxygen evolution, *Adv. Energy Mater.* 12 (2022) 2202522, <https://doi.org/10.1002/aenm.202202522>.
- [34] H. Wang, L. Chen, L. Tan, X. Liu, Y. Wen, W. Hou, T. Zhan, Electrodeposition of NiFe-layered double hydroxide layer on sulfur-modified nickel molybdate nanorods for highly efficient seawater splitting, *J. Colloid Inter. Sci.* 613 (2022) 349–357, <https://doi.org/10.1016/j.jcis.2022.01.044>.
- [35] J. Zhao, Z. Shi, C. Li, L. Gu, G. Li, Boosting the electrocatalytic performance of NiFe layered double hydroxides for the oxygen evolution reaction by exposing the highly active edge plane (012), *Chem. Sci.* 12 (2021) 650–659, <https://doi.org/10.1039/D0SC04196C>.
- [36] H. Xiao, H. Shin, W. Goddard, Synergy between Fe and Ni in the optimal performance of (Ni,Fe)OOH catalysts for the oxygen evolution reaction, *Proc. Natl. Acad. Sci.* 115 (2018) 5872–5877, <https://doi.org/10.1073/pnas.1722034115>.
- [37] Z. Wang, C. Wang, L. Ye, X. Liu, L. Xin, Y. Yang, W. Hou, Y. Wen, T. Zhan, MnO_x Film-Coated NiFe-LDH nanosheets on Ni foam as selective oxygen evolution electrocatalysts for alkaline seawater oxidation, *Inorg. Chem.* 61 (2022) 15256–15265, <https://doi.org/10.1021/acs.inorgchem.2c02579>.
- [38] J. Han, X. Meng, L. Lu, Z. Wang, C. Sun, Triboelectric nanogenerators powered electrodeposition tri-functional electrocatalysts for water splitting and rechargeable zinc-air battery: a case of Pt nanoclusters on NiFe-LDH nanosheets, *Nano Energy* 72 (2020), 104669, <https://doi.org/10.1016/j.nanoen.2020.104669>.
- [39] P. Thiel, T. Madey, The interaction of water with solid surfaces: fundamental aspects, *Surf. Sci. Rep.* 7 (1987) 211–385, [https://doi.org/10.1016/0167-5729\(87\)90001-X](https://doi.org/10.1016/0167-5729(87)90001-X).
- [40] Y. Li, Y. Sun, Y. Qin, W. Zhang, L. Wang, M. Luo, H. Yang, S. Guo, Recent advances on water-splitting electrocatalysis mediated by noble-metal-based nanostructured materials, *Adv. Energy Mater.* 10 (2020) 1903120, <https://doi.org/10.1002/aenm.201903120>.
- [41] Y. Guo, B. Hou, X. Cui, X. Tong, T. Yang, Pt atomic layers boosted hydrogen evolution reaction in nonacidic media, *Adv. Energy Mater.* 12 (2022) 2201548, <https://doi.org/10.1002/aenm.202201548>.
- [42] F. Yang, Y. Zhao, Y. Du, Y. Chen, G. Cheng, S. Chen, W. Luo, A. Monodisperse, Rh₂P-based electrocatalyst for highly efficient and pH-Universal hydrogen evolution reaction, *Adv. Energy Mater.* 8 (2018) 1703489, <https://doi.org/10.1002/aenm.201703489>.
- [43] T. Liu, X. Ma, D. Liu, S. Hao, G. Du, Y. Ma, A. Asiri, X. Sun, L. Chen, Mn Doping of CoP nanosheets array: an efficient electrocatalyst for hydrogen evolution reaction

- with enhanced activity at all pH values, *ACS Catal.* 7 (2017) 98–102, <https://doi.org/10.1021/acscatal.6b02849>.
- [44] F. Luo, L. Guo, Y. Xie, J. Xu, K. Qu, Z. Yang, Iridium nanorods as a robust and stable bifunctional electrocatalyst for pH-universal water splitting, *Appl. Catal. B* 279 (2020), 119394, <https://doi.org/10.1016/j.apcatb.2020.119394>.
- [45] S. Anantharaj, K. Karthick, M. Venkatesh, T. Simha, A. Salunke, L. Ma, H. Liang, S. Kundu, Enhancing electrocatalytic total water splitting at few layer Pt-NiFe layered double hydroxide interfaces, *Nano Energy* 39 (2017) 30–43, <https://doi.org/10.1016/j.nanoen.2017.06.027>.
- [46] Y. Zhao, Y. Gao, Z. Chen, Z. Li, T. Ma, X. Ma, X. Wu, L. Wang, Trifunctional Pt coupled with NiFe hydroxide synthesized via corrosion engineering to boost the cleavage of water molecule for alkaline water-splitting, *Appl. Catal. B* 297 (2021), 120395, <https://doi.org/10.1016/j.apcatb.2021.120395>.
- [47] Y. Bai, Y. Wu, X. Zhou, Y. Ye, K. Nie, J. Wang, M. Xie, Z. Zhang, Z. Liu, T. Cheng, C. Gao, Promoting nickel oxidation state transitions in single-layer NiFeB hydroxide nanosheets for efficient oxygen evolution, *Nat. Commun.* 13 (2022) 6094, <https://doi.org/10.1038/s41467-022-33846-0>.
- [48] J. Li, Y. Liu, H. Chen, Z. Zhang, X. Zou, Design of a multilayered oxygen-evolution electrode with high catalytic activity and corrosion resistance for saline water splitting, *Adv. Funct. Mater.* 31 (2021) 2101820, <https://doi.org/10.1002/adfm.202101820>.
- [49] H. Li, X. Qin, X. Zhang, K. Jiang, W. Bai, Boron-doped platinum-group metals in electrocatalysis: a perspective, *ACS Catal.* 12 (2022) 12750–12764, <https://doi.org/10.1021/acscatal.2c04358>.
- [50] X. Wang, X. Wan, X. Qin, C. Chen, X. Qian, Y. Guo, Q. Xu, W. Cai, H. Yang, K. Jiang, Electronic structure modulation of RuO₂ by TiO₂ enriched with oxygen vacancies to boost acidic O₂ evolution, *ACS Catal.* 12 (2022) 9437–9445, <https://doi.org/10.1021/acscatal.2c01944>.
- [51] Z. Mao, C. Ding, X. Liu, Q. Zhang, X. Qin, H. Li, F. Yang, Q. Li, X. Zhang, W. Bai, Interstitial B-Doping in Pt lattice to upgrade oxygen electroreduction performance, *ACS Catal.* 12 (2022) 8848–8856, <https://doi.org/10.1021/acscatal.2c01052>.
- [52] D. Li, X. Chen, Y. Lv, G. Zhang, Y. Huang, W. Liu, Y. Li, R. Chen, C. Nuckolls, H. Ni, An effective hybrid electrocatalyst for the alkaline HER: highly dispersed Pt sites immobilized by a functionalized NiRu-hydroxide, *Appl. Catal. B* 269 (2020), 118824, <https://doi.org/10.1016/j.apcatb.2020.118824>.
- [53] J. Wu, Z. Nie, R. Xie, X. Hu, Y. Yu, N. Yang, Self-assembled Pt–CoFe layered double hydroxides for efficient alkaline water/seawater splitting by spontaneous redox synthesis, *J. Power Sources* 532 (2022), 231353, <https://doi.org/10.1016/j.jpowsour.2022.231353>.
- [54] L. Wu, L. Yu, F. Zhang, D. Wang, D. Luo, S. Song, C. Yuan, A. Karim, S. Chen, Z. Ren, Facile synthesis of nanoparticle-stacked tungsten-doped nickel iron layered double hydroxide nanosheets for boosting, *Oxyg. Evol. React. J. Mater. Chem. A* 8 (2020) 8096–8103, <https://doi.org/10.1039/D0TA00691B>.
- [55] X. Yu, Y. Kang, S. Wang, K.S. Hui, K.N. Hui, H. Zhao, J. Li, B. Li, J. Xu, L. Chen, H. Shao, Integrating PtNi nanoparticles on NiFe layered double hydroxide nanosheets as a bifunctional catalyst for hybrid sodium–air, *Batter. J. Mater. Chem. A* 8 (2020) 16355–16365, <https://doi.org/10.1039/D0TA04602G>.
- [56] M. Zolopa, E. Gradzka, K. Szymanski, K. Winkler, Electrodeposition of nickel, cobalt, and iron on polypyrrole films, *Thin Solid Films* 548 (2013) 44–51, <https://doi.org/10.1016/j.tsf.2013.08.082>.
- [57] T. Zhai, S. Sun, X. Liu, C. Liang, G. Wang, H. Xia, Achieving insertion-like capacity at ultrahigh rate via tunable surface pseudocapacitance, *Adv. Mater.* 30 (2018) 1706640, <https://doi.org/10.1002/adma.201706640>.
- [58] S. Sun, T. Zhai, C. Liang, S. Savilov, H. Xia, Boosted crystalline/amorphous Fe₂O_{3-δ} core/shell heterostructure for flexible solid-state pseudocapacitors in large scale, *Nano Energy* 45 (2018) 390–397, <https://doi.org/10.1016/j.nanoen.2018.01.015>.
- [59] L. Wu, L. Yu, Q. Zhu, B. McElhenny, F. Zhang, C. Wu, X. Xing, J. Bao, S. Chen, Z. Ren, Boron-modified cobalt iron layered double hydroxides for high efficiency seawater oxidation, *Nano Energy* 83 (2021), 105838, <https://doi.org/10.1016/j.nanoen.2021.105838>.
- [60] H. Yang, Z. Chen, P. Guo, B. Fei, R. Wu, B-doping-induced amorphization of LDH for large-current-density hydrogen evolution reaction, *Appl. Catal. B* 261 (2020), 118240, <https://doi.org/10.1016/j.apcatb.2019.118240>.
- [61] X. Li, C. Liu, Z. Fang, L. Xu, C. Lu, W. Hou, Ultrafast room-temperature synthesis of self-supported NiFe-layered double hydroxide as large-current-density oxygen evolution electrocatalyst, *Small* 18 (2022) 2104354, <https://doi.org/10.1002/smll.202104354>.
- [62] Y. Li, Y. Wu, H. Hao, M. Yuan, Z. Lv, L. Xu, B. Wei, In situ unraveling surface reconstruction of Ni₅P₄@FeP nanosheet array for superior alkaline oxygen evolution reaction, *Appl. Catal. B* 305 (2022), 121033, <https://doi.org/10.1016/j.apcatb.2021.121033>.
- [63] M. Iqbal, K. Shahzad, R. Akbar, G. Hussain, A review on Raman finger prints of doping and strain effect in TMDs, *Micro Eng.* 219 (2020), 111152, <https://doi.org/10.1016/j.mee.2019.111152>.
- [64] Q. Lei, L. Huang, J. Yin, B. Davaasuren, Y. Yuan, X. Dong, Z. Wu, X. Wang, K. Yao, X. Lu, Y. Han, Structural evolution and strain generation of Derived-Cu catalysts during CO₂ electroreduction, *Nat. Commun.* 13 (2022) 4857, <https://doi.org/10.1038/s41467-022-32601-9>.
- [65] X. Long, G. Li, Z. Wang, H. Zhu, T. Zhang, S. Xiao, W. Guo, S. Yang, Metallic iron–nickel sulfide ultrathin nanosheets as a highly active electrocatalyst for hydrogen evolution reaction in acidic media, *J. Am. Chem. Soc.* 137 (2015) 11900–11903, <https://doi.org/10.1021/jacs.5b07728>.
- [66] Y. Kang, Y. Guo, J. Zhao, B. Jiang, J. Guo, Y. Tang, H. Li, V. Malgras, M. Amin, H. Nara, Y. Sugahara, Y. Yamuchi, T. Asahi, Soft template-based synthesis of mesoporous phosphorus- and boron-codoped nife-based alloys for efficient oxygen evolution reaction, *Small* 18 (2022) 2203411, <https://doi.org/10.1002/smll.202203411>.
- [67] V. Saveleva, V. Papaefthimiou, M. Daletou, W. Doh, C. Ulhaq-Bouillet, M. Diebold, S. Zafeirotas, E. Savinova, Operando near ambient pressure XPS (NAP-XPS) study of the Pt electrochemical oxidation in H₂O and H₂O/O₂ ambients, *J. Phys. Chem. C* 120 (2016) 15930–15940, <https://doi.org/10.1021/acs.jpcc.5b12410>.
- [68] P. Kuang, Y. Wang, B. Zhu, F. Xia, C. Tung, J. Wu, H. Chen, J. Yu, Pt Single atoms supported on N-doped mesoporous hollow carbon spheres with enhanced electrocatalytic H₂-Evolution activity, *Adv. Mater.* 33 (2021) 2008599, <https://doi.org/10.1002/adma.202008599>.
- [69] J. Su, Y. Yang, G. Xia, J. Chen, P. Jiang, Q. Chen, Ruthenium-cobalt nanoalloys encapsulated in nitrogen-doped graphene as active electrocatalysts for producing hydrogen in alkaline media, *Nat. Commun.* 8 (2017) 14969, <https://doi.org/10.1038/ncomms14969>.
- [70] M. Nath, J. Masud, A. Swesi, T. Energy, E. Ees, Nickel selenide as a high-efficiency catalyst for oxygen evolution reaction, *Energy Environ. Sci.* 9 (2016) 1771–1782, <https://doi.org/10.1039/C5EE02463C>.
- [71] A. Garcia, T. Touzalin, C. Nieuwland, N. Perini, M. Koper, Enhancement of oxygen evolution activity of nickel oxyhydroxide by electrolyte alkali cations, *Angew. Chem. Int. Ed.* 58 (2019) 12999–13003, <https://doi.org/10.1002/anie.201905501>.
- [72] D. Chung, P. Lopes, P. Farinazzo, H. He, T. Kawaguchi, P. Zapol, H. You, D. Tripkovic, D. Strmcnik, Y. Zhu, S. Seifert, S. Lee, V. Stamenkovic, N. Markovic, Dynamic stability of active sites in Hydr(oxy)oxides for the oxygen evolution reaction, *Nat. Energy* 5 (2020) 222–230, <https://doi.org/10.1038/s41560-020-0576-y>.
- [73] F. Dionigi, Z. Zeng, I. Sinev, T. Merzdorf, S. Deshpande, M. Lopez, S. Kunze, I. Zegkinoglou, H. Sarodnik, D. Fan, A. Bergmann, J. Drnec, J. Araujo, H. Gliech, D. Teschner, J. Zhu, W. Li, J. Greeley, B. Cuenya, P. Strasser, In-situ structure and catalytic mechanism of NiFe and CoFe layered double hydroxides during oxygen evolution, *Nat. Commun.* 11 (2020) 2522, <https://doi.org/10.1038/s41467-020-16237-1>.
- [74] Y. Shi, Z. Ma, Y. Xiao, Y. Yin, W. Huang, Z. Huang, Y. Zheng, F. Mu, R. Huang, G. Shi, Y. Sun, X. Xia, W. Chen, Electronic metal–support interaction modulates single-atom platinum catalysis for hydrogen evolution reaction, *Nat. Commun.* 12 (2021) 3021, <https://doi.org/10.1038/s41467-021-23306-6>.
- [75] X. Fu, D. Cheng, C. Wan, S. Kumari, H. Zhang, A. Zhang, H. Huyen, J. Zhou, H. Ren, S. Wang, Z. Zhao, X. Zhao, J. Chen, X. Pan, P. Sautet, Y. Huang, X. Duan, Bifunctional ultrathin RhRu_{0.5}-alloy nanowire electrocatalysts for hydrazine-assisted water splitting, *Adv. Mater.* 35 (2023) 2208209, <https://doi.org/10.1002/adma.202301533>.
- [76] H. Zhang, P. Shi, X. Ma, C. Ma, S. Han, C. He, H. Wu, L. Zhu, B. Zhang, Y. Lu, W. Cao, H. Yin, X. Meng, J. Xia, J. Zhang, A. Wang, Q. Lu, Construction of ordered atomic donor–acceptor architectures in bcc IrGa intermetallic compounds toward highly electroactive and stable overall water splitting, *Adv. Energy Mater.* 13 (2023) 2202703, <https://doi.org/10.1002/aenm.202202703>.
- [77] Y. Yang, Y. Kang, H. Zhao, X. Dai, M. Cui, X. Luan, X. Zhang, F. Nie, Z. Ren, W. Song, An interfacial electron transfer on tetrahedral NiS₂/NiSe₂ heterocages with dual-phase synergy for efficiently triggering the oxygen evolution reaction, *Small* 16 (2019) 1905083, <https://doi.org/10.1002/smll.201905083>.
- [78] K. Lu, Y. Liu, F. Lin, L. Cordova, S. Gao, B. Li, B. Peng, H. Xu, J. Kaelin, D. Coliz, C. Wang, Y. Shao, Y. Cheng, Li_xNiO/Ni heterostructure with strong basic lattice oxygen enables electrocatalytic hydrogen evolution with Pt-like activity, *J. Am. Chem. Soc.* 142 (2020) 12613–12619, <https://doi.org/10.1021/jacs.0c00241>.
- [79] R. Subbaraman, D. Tripkovic, D. Strmcnik, K. Chang, M. Uchimura, A. Paulikas, V. Stamenkovic, N. Markovic, Enhancing hydrogen evolution activity in water splitting by tailoring Li⁺-Ni(OH)₂-Pt interfaces, *Science* 334 (2011) 1256–1260, <https://doi.org/10.1126/science.1211934>.
- [80] X. Guo, X. Wan, Q. Liu, Y. Li, W. Li, J. Shui, Phosphated IrMo bimetallic cluster for efficient hydrogen evolution reaction, *eScience* 2 (2022) 304–310, <https://doi.org/10.1016/j.esci.2022.04.002>.
- [81] B. Fei, Z. Chen, J. Liu, H. Xu, X. Yan, H. Qing, M. Chen, R. Wu, Ultrathinning nickel sulfide with modulated electron density for efficient water splitting, *Adv. Energy Mater.* 10 (2020) 2001963, <https://doi.org/10.1002/aenm.202001963>.
- [82] Y. Lin, Z. Tian, L. Zhang, J. Ma, Z. Jiang, B. Deibert, R. Ge, L. Chen, Chromium–ruthenium oxide solid solution electrocatalyst for highly efficient oxygen evolution reaction in acidic media, *Nat. Commun.* 10 (2019) 162, <https://doi.org/10.1038/s41467-018-08144-3>.
- [83] C. Dinh, A. Jain, F. Arquer, P. Luna, J. Li, N. Wang, X. Zheng, J. Cai, B. Gregory, O. Voznyy, B. Zhang, M. Liu, D. Sinton, E. Crumlin, E. Sargent, Multi-site electrocatalysts for hydrogen evolution in neutral media by destabilization of water molecules, *Nat. Energy* 4 (2019) 107–114, <https://doi.org/10.1038/s41560-018-0296-8>.